Supporting Information for

A Transferrable, Adaptable, Free-Standing, and Water-Resistant Hyperbolic Metamaterial

Hung-I Lin[1], Hsiang-Yao Tan[1], Yu-Ming Liao[1], Kun-Ching Shen[2], Mikhail Y. Shalaginov[3], Monika Kataria[1], Chih-Ting Chen[1], Jun-Wei Chang[1], and Yang-Fang Chen[1,4]*

[1] Department of Physics, National Taiwan University, Taipei 10617, Taiwan

[2] Advanced Remanufacturing and Technology Centre, The Agency for Science, Technology and Research, Singapore

[3] Department of Materials Science and Engineering, Massachusetts Institute of Technology, 77 Massachusetts Avenue, Cambridge, MA 02139, USA

[4] Advanced Research Centre for Green Materials Science and Technology, National Taiwan University, Taipei 10617, Taiwan

*corresponding author: Yang-Fang Chen: yfchen@phys.ntu.edu.tw

1. Fabrication processes of grating collageable hyperbolic metamaterial (GCHMM) and planar collageable hyperbolic metamaterial (PCHMM).

The GCHMM is composed of grating structure with poly(methylmethacrylate) (PMMA) embedded CdSe/ZnS QDs and 4 pairs of PMMA (30 nm)/Au film (12 nm). The fabrication processes of the GCHMM is shown in Fig. S1. First, we spin-coated polyvinyl alcohol (PVA) solution onto the grating substrate to mold the patterns. After curing the PVA, we peeled it off from the grating substrate and then transferred it on the silicon (Si) substrate (*i.e.*, PVA grating structure). Next, we mixed QDs with PMMA. After mixing, the solution was spin-coated onto the PVA grating structure, and it was heated at 80 ^{0}C for 30 min. To fabricate multilayers of HMM structure, we spin-coated PMMA onto the grating structure at the rate of 4000 rpm, and then we heated it at 80 ^{0}C for 30 min to cure PMMA. Then, Au thin film was deposited by thermal evaporation system under the chamber pressure of 2 x 10^{-6} Torr and the deposition rate was 0.3 Å/s. After repeating the above-mentioned processes for 3 times, we finished the fabrication of multilayers of HMM structure. Afterwards, we put the whole structure upside down on the Si or any other substrate to expose the PVA grating structure on the top. Finally, we drop the distilled (DI) water on the whole structure to dissolve the PVA grating structure to obtain the GCHMM. The CdSe/ZnS core-shell type QDs with the emission wavelength center at 630 nm is commercially available (Sigma-Aldrich).

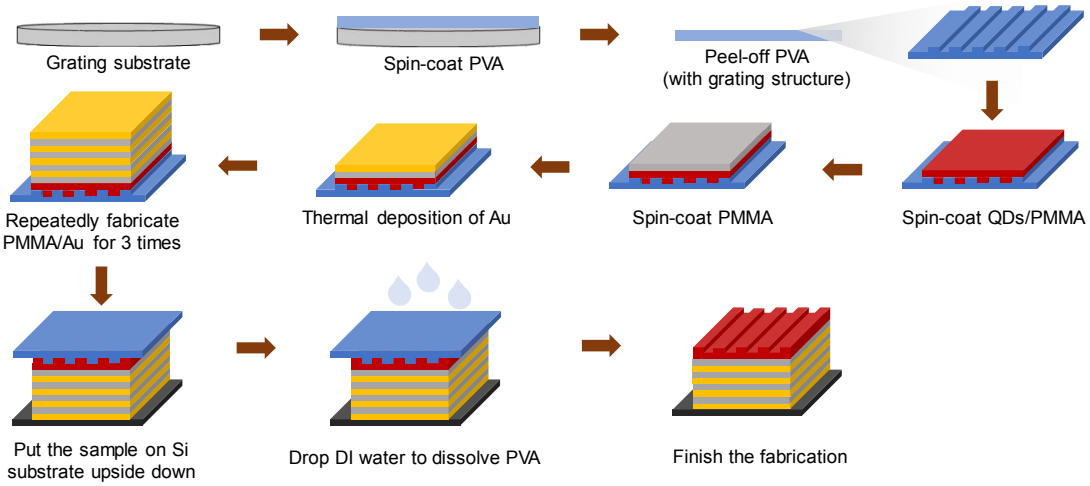

Figure S1 | Fabrication processes of the GCHMM.

The PCHMM is composed of planar PMMA embedded CdSe/ZnS QDs and 4 pairs of PMMA (30 nm)/Au film (12 nm). The fabrication processes of the PCHMM is shown in Fig. S2. First, we spin-coated PVA on the Si substrate and heated it to form PVA thin film. Then, we spin-coated PMMA embedded with QDs onto the PVA film. To fabricate multilayers of HMM structure, we spin-coated PMMA at the rate of 4000 rpm, and then we heated it at 80 ^{o}C for 30 min to cure PMMA. Then, Au thin film was deposited by thermal evaporation system under the chamber pressure of 2 x 10^{-6} Torr and the deposition rate was 0.3 Å/s. After repeating the above-mentioned processes for 3 times, we finished the fabrication of multilayers of HMM structure. Afterwards, we put the whole structure upside down on the Si or any other substrate to expose the PVA grating structure on the top. Finally, we drop the DI water on the whole structure to dissolve the PVA grating structure to obtain the PCHMM.

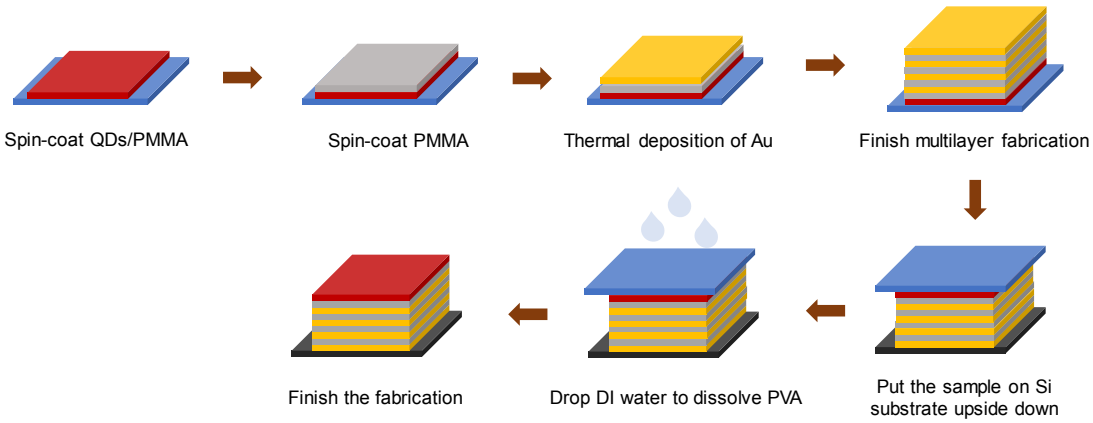

Figure S2 | Fabrication processes of the PCHMM.

2. SEM image of PCHMM.

Figure S3 shows the cross-sectional view of scanning electron microscopy (SEM) image of free-standing PCHMM. The HMM is composed of 4 pairs of flexible Au/PMMA multilayers with thickness of 12/30 nm. The CdSe/ZnS core-shell type QDs are embedded inside the PMMA as the planar layer.

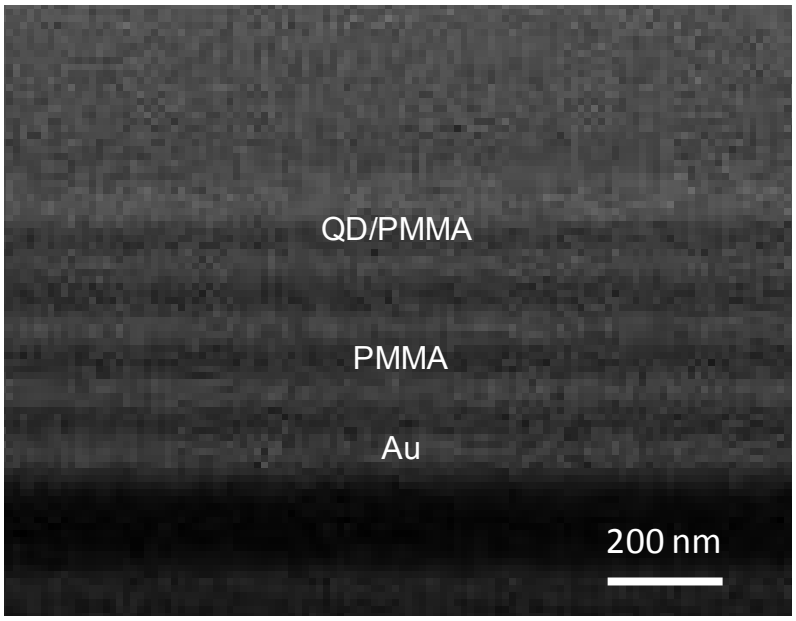

Figure S3 | The cross-sectional view of SEM image of PCHMM. The HMM is composed of 4 pairs of flexible Au/PMMA multilayers with thickness of 12/30 nm. The CdSe/ZnS core-shell type QDs are embedded inside the PMMA as the planar layer.

3. High-resolution transmission electron microscopy (HR-TEM) of CdSe/ZnS QDs.

Figure S4 shows the HR-TEM of CdSe/ZnS QDs. The average diameter is ~6 nm.

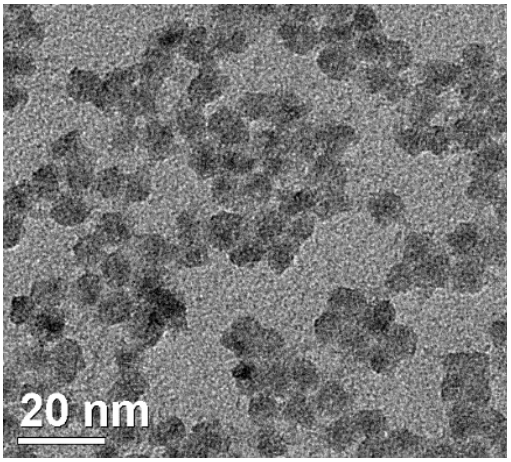

Figure S4 | The HR-TEM image of CdSe/ZnS QDs.

4. Hyperbolic-dispersion calculations.

The calculation of effective medium theory is realized as follows. Since the thicknesses of Au and PMMA layers (12 nm and 30 nm, respectively) are much smaller than the wavelength of interest (630 nm), then we can consider the homogeneity of effective permittivity tensors and consider the structure as the effective medium theory (EMT). Therefore, the parallel ($\varepsilon_{\parallel}$) and perpendicular ($\varepsilon_{\perp}$) effectives to the surface of HMM are determined as:[1]

$$\varepsilon_{\parallel} = \varepsilon_x = \varepsilon_y = \sum_{n=1}^{2} f_n \varepsilon_n, \tag{S1}$$

$$\varepsilon_{\perp}^{-1} = \varepsilon_z^{-1} = \sum_{n=1}^{2} f_n \varepsilon_n^{-1}, \tag{S2}$$

$$f_n = \frac{d_n}{\sum_{n=1}^{2} d_n}, \tag{S3}$$

where f_n is the fill fraction of the layer component, and d_n is the thickness of the n-the layer of the multilayer structure. The dielectric tensor components are further determined as:

$$\varepsilon_{\perp} = \rho\varepsilon_{Au} + (1-\rho)\varepsilon_{PMMA}, \tag{S4}$$

and

$$\varepsilon_{\parallel} = \frac{(1-\rho)\varepsilon_{Au}\varepsilon_{PMMA} + (1+\rho)\varepsilon_{PMMA}^2}{(1-\rho)\varepsilon_{Au} + (1+\rho)\varepsilon_{PMMA}}, \tag{S5}$$

where ρ is the fill fraction of the metal component of the multilayer structure. Then, the hyperbolic dispersion ($\varepsilon_{\perp} \cdot \varepsilon_{\parallel} < 0$) can be furtherly determined.

Figure S5 shows the effective dielectric tensor calculation of the HMM. Light green region (wavelength range below 555 nm) is the elliptical dispersion ($\varepsilon_{\perp} \cdot \varepsilon_{\parallel} > 0$) and light blue region (wavelength range above 555 nm) is the hyperbolic dispersion ($\varepsilon_{\perp} \cdot \varepsilon_{\parallel} < 0$) in the wavelength region of 400 nm to 1000 nm.

The hyperbolic dispersion of HMM ($\varepsilon_\perp \cdot \varepsilon_\parallel < 0$) is determined from the effective medium theory from the optical tensors (in Fig. 2a):[2]

$$\frac{\omega^2}{c^2} = \frac{k_x^2 + k_y^2}{\varepsilon_\parallel} + \frac{k_z^2}{\varepsilon_\perp}, \tag{S6}$$

where ω is the angular frequency; k_x, k_y, and k_z are the component of the wavevector along x, y, and z axis, respectively; and c is the speed of light in vacuum.

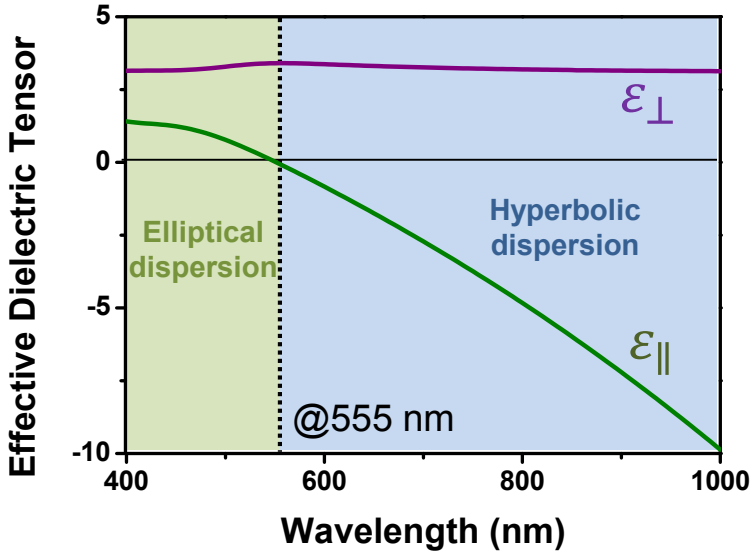

Figure S5 | Hyperbolic-dispersion calculations. The effective dielectric tensor calculation of the HMM. Light green region (wavelength range below 555 nm) is the elliptical dispersion ($\varepsilon_\perp \cdot \varepsilon_\parallel > 0$) and light blue region (wavelength range above 555 nm) is the hyperbolic dispersion ($\varepsilon_\perp \cdot \varepsilon_\parallel < 0$) in the wavelength region of 400 nm to 1000 nm.

5. Normalized dissipated power spectra.

Furthermore, to determine the normalized dissipated power spectra (in Fig. 2b), the discussion of Purcell factor is essential. When a dipole emitter is placed on top of the surface of sample with a perpendicular ($\perp$) and parallel ($\parallel$) orientation, the Purcell factor (F) is determined as:[3, 4]

$$F_{\perp} = 1 - \eta_0 + \frac{3}{2}\eta_0 \mathrm{Re}\int_0^{\infty} \mathrm{d}k_x \frac{1}{k_z}\left(\frac{k_x}{\sqrt{\varepsilon_1}k_0}\right)^3 \left[1 + r_P e^{2ik_z d}\right] \quad \text{(S7)}$$

$$F_{\parallel} = 1 - \eta_0 + \frac{3}{4}\eta_0 \mathrm{Re}\int_0^{\infty} \mathrm{d}k_x \frac{1}{k_z\sqrt{\varepsilon_1}k_0}\left\{1 + r_S e^{2ik_z d} + \frac{{k_z}^2}{\varepsilon_1 {k_0}^2}\left[1 - r_P e^{2ik_z d}\right]\right\} \quad \text{(S8)}$$

where d is the distance of dipole emitter to the surface; η_0 is the internal quantum efficiency of QDs in free space ($\eta_0 = 1$); r_P and r_S are the reflection coefficients for P- or S-polarized waves at the interfaces, respectively. Then, the integrants of Equations (S1) and (S2) are the normalized dissipated power spectra:

$$\frac{\mathrm{d}P_{\perp}}{\mathrm{d}k_x} = \frac{3}{2}\frac{1}{k_z}\left(\frac{k_x}{\sqrt{\varepsilon_1}k_0}\right)^3 \left[1 + r_P e^{2ik_z d}\right] \quad \text{(S9)}$$

$$\frac{dP_p}{dk_x} = \frac{3}{4}\frac{1}{k_z\sqrt{\varepsilon_1}k_0}\left\{1 + r_S e^{2ik_z d} + \frac{{k_z}^2}{\varepsilon_1 {k_0}^2}\left[1 - r_P e^{2ik_z d}\right]\right\} \quad \text{(S10)}$$

Figure S6 shows the normalized dissipated power spectrum without considering loss effect from the Au composition of HMM at the dipole distance away from the substrate within 5 nm.

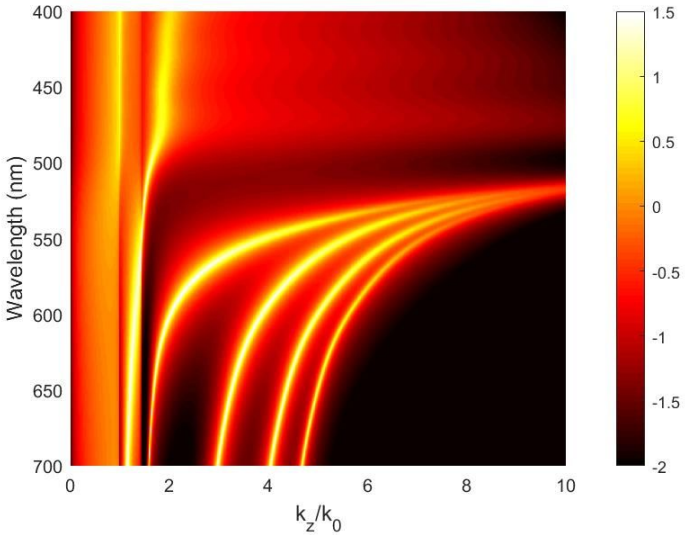

Figure S6 | The normalized dissipated power spectrum without considering loss effect from the Au composition of HMM at the dipole distance away from the substrate of 5 nm. The spectrum is plotted in logarithmic scale.

Figure S7 shows the normalized dissipated power spectra with and without considering loss effect from the Au composition of HMM at the dipole distance away from the substrate of 10 nm, 15 nm, and 20 nm.

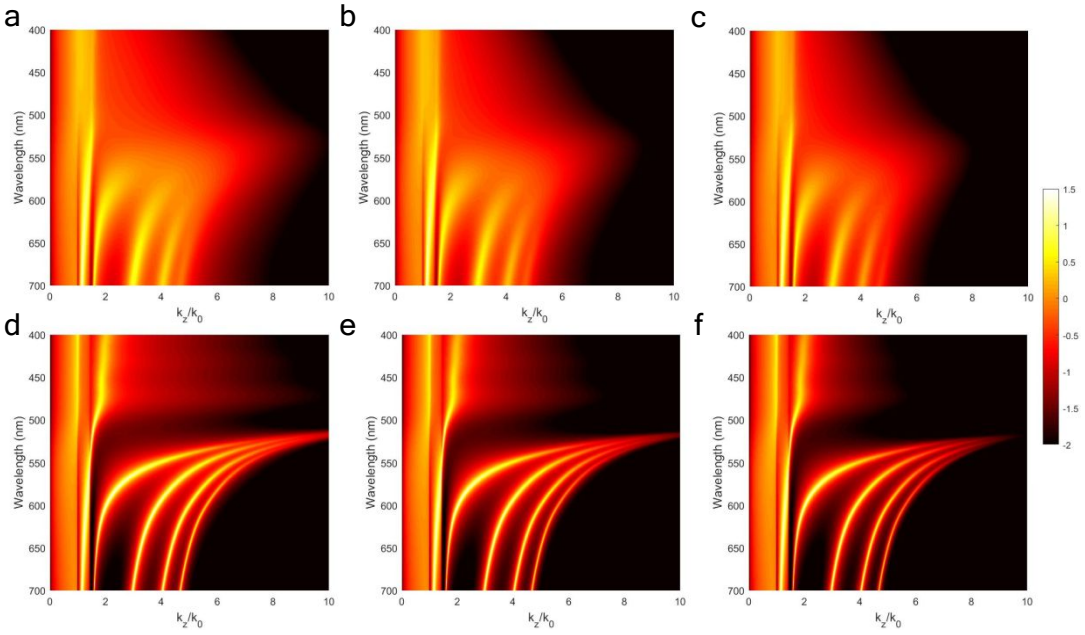

Figure S7 | The normalized dissipated power spectra with considering loss effect from the Au composition of HMM at the dipole distance away from the substrate of (a) 10 nm, (b) 15 nm, and (c) 20 nm. (d-f) are the corresponding spectra without considering the loss effect.

6. The area of incident laser spot.

Figure S8 shows the schematic diagrams of the measurements through the optical microscope system with the 100× objective lens (Olympus, Japan) with the numerical aperture ($N.A$) of 0.9. According to the Gaussian beam theory, when the incident laser source passing through an objective lens, the radius (r) of the laser spot:

$$r = \frac{1.22\lambda}{N.A} \tag{S11}$$

where λ is the wavelength of incident laser source (*e.g.*, 374 nm). The radius of the incident laser spot is ~507 nm.

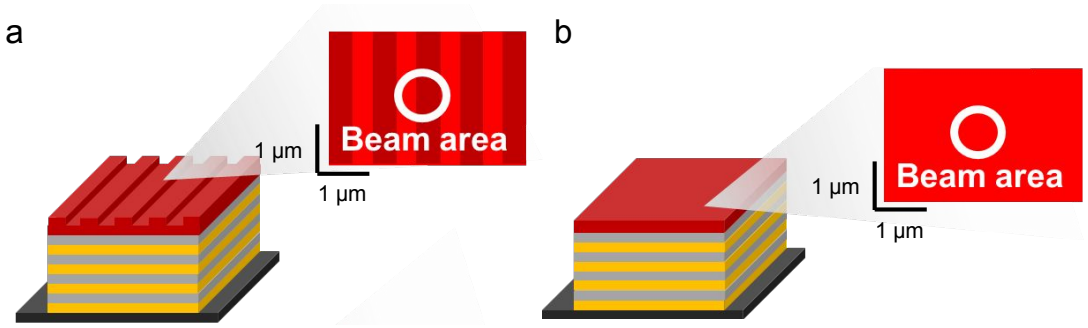

Figure S8 | The schematic diagrams of the measurements through the optical microscope system with the 100× objective lens (Olympus, Japan) with the numerical aperture of 0.9 for (a) GCHMM and (b) PCHMM. The radius of the incident laser spot is ~507 nm.

7. Emission spectra of random laser action.

Figures S9a and S9b show the emission spectra of CdSe/ZnS QDs embedded inside the planar CHMM (PCHMM) and on Si substrate, respectively. Three kinds of pumping energy densities are performed to discover the random laser action. For the PCHMM, under the pumping energy density of 1.12 kW cm^{-2}, the typical spontaneous emission is observed. With further increasing the pumping energy densities to 2.13 and 2.95 kW cm^{-2}, the random laser action with clearly sharp peaks are emerged. For the pure CdSe/ZnS QDs on Si substrate, under these three kinds of pumping energy densities, the spectra are spontaneous emissions.

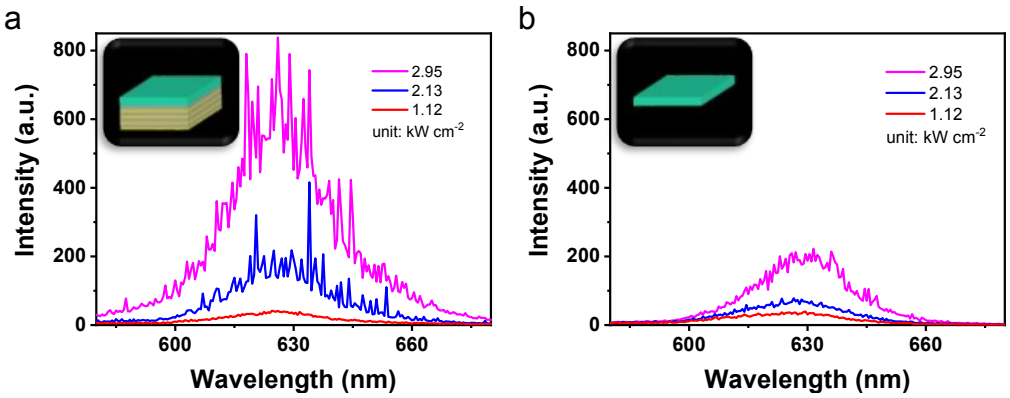

Figure S9 | (a) and (b) are the emission spectra of CdSe/ZnS QDs embedded inside the planar CHMM (PCHMM) and on Si substrate, respectively. The insets are the corresponding schemes.

8. Calculations of the performances of GCHMM.

The detailed calculations to obtain the performances of GCHMM are as follows (Table S1).

	Emission intensity (a.u.)	Threshold (kW cm^{-2})	Slope of laser action (a.u./ kW cm^{-2})
GCHMM	64	1.05	4.45
PCHMM	896	1.95	1.57
Performances of GCHMM	13 times enhancement	46% reduced	1.8-fold increase in differential quantum efficiency[5]

Table S1 | The detailed calculations to obtain the performances of GCHMM.

9. Lifetime measurements.

Figures S10a, S10b and S10c show the lifetime measurements for GCHMM, PCHMM and planar PMMA, respectively.

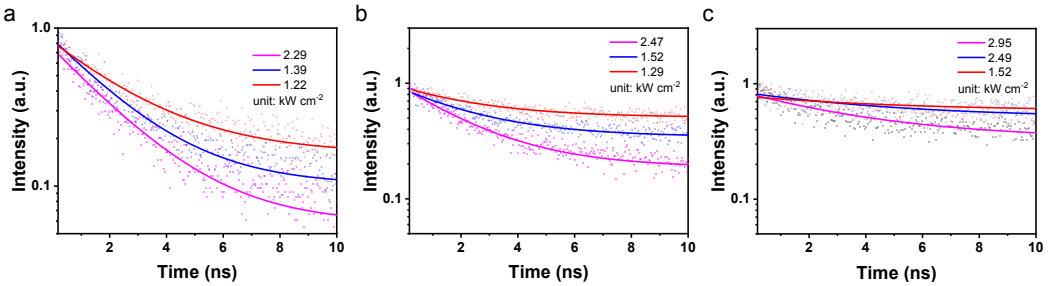

Figure S10 | (a), (b) and (c) are the lifetime measurements for GCHMM, PCHMM and planar PMMA, respectively.

10. Broad angular emissions.

Figures S11 and S12 show the emission spectra of random lasing action measured at the tilted sample holder up to 20° for grating CHMM (GCHMM) and PCHMM, respectively. The simulated normalized intensity of far-field angular emission is shown in Fig. S13.

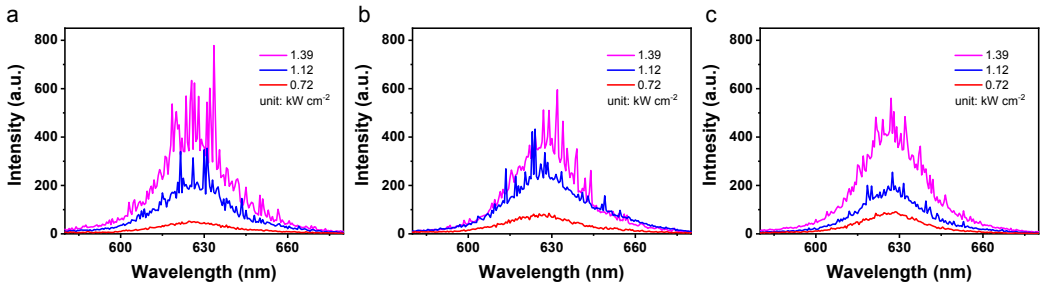

Figure S11 | (a), (b) and (c) are the emission spectra for the GCHMM at the tilted sample holder of normal, 10° and 20°, respectively.

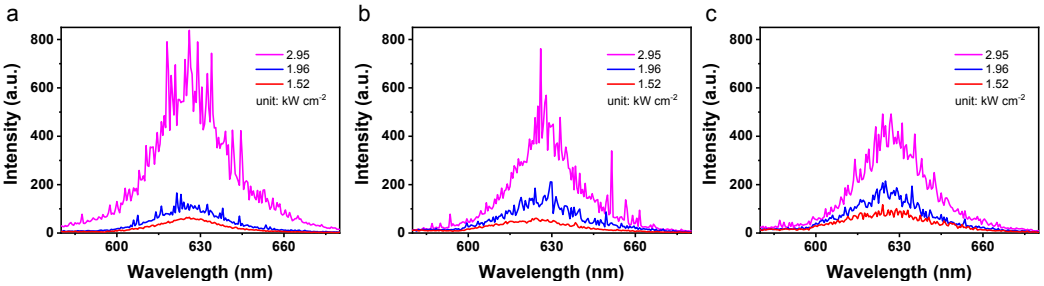

Figure S12 | (a), (b) and (c) are the emission spectra for the PCHMM at the tilted sample holder of normal, 10° and 20°, respectively.

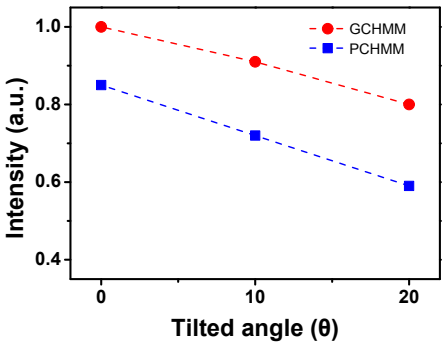

Figure S13 | The normalized intensity of far-field angular emission at the center position of far-field monitor from normal to the tilted incident angles of 20°.

11. Purcell factors.

Figures S14a and S14b are the Purcell factors for the perpendicular dipole ($F_{\perp}$) and parallel dipole ($F_{\parallel}$) away from the multilayer HMM structure, respectively. The Purcell factors with isotropic dipole orientations (F_{iso}) are:

$$F_{iso} = \frac{1}{3}F_{\perp} + \frac{2}{3}F_{\parallel}. \tag{S12}$$

To observe the different effects of dipole orientations to the multilayer HMM structure, we plotted the $F_{\perp}$ and $F_{\parallel}$ separately.

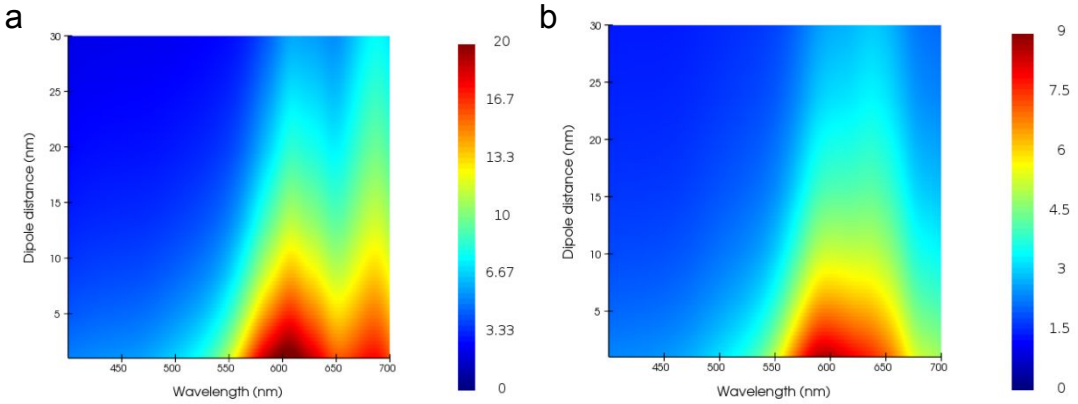

Figure S14 | (a) and (b) are the Purcell factors for the perpendicular and parallel dipoles away from the multilayer HMM structure, respectively.

12. Time decay of electric-field intensities.

Figures S15 shows the time decay of electric-field intensities with the corresponding envelopes for the GCHMM and PCHMM.

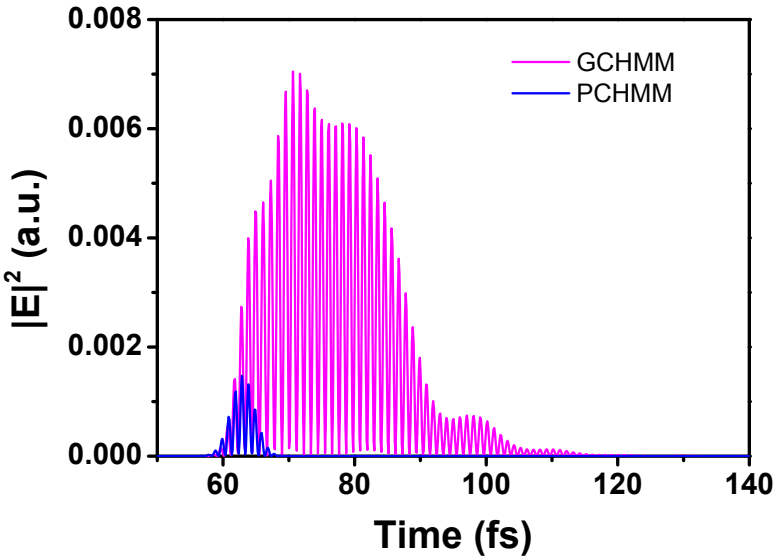

Figure S15 | The time decay of electric-field intensities with the corresponding envelopes for the GCHMM and PCHMM.

13. Emission performances under different curvature radiuses.

Figures S16 shows the emission performances on concave and convex glass substrates under different curvature radiuses of 20 mm and 50 mm.

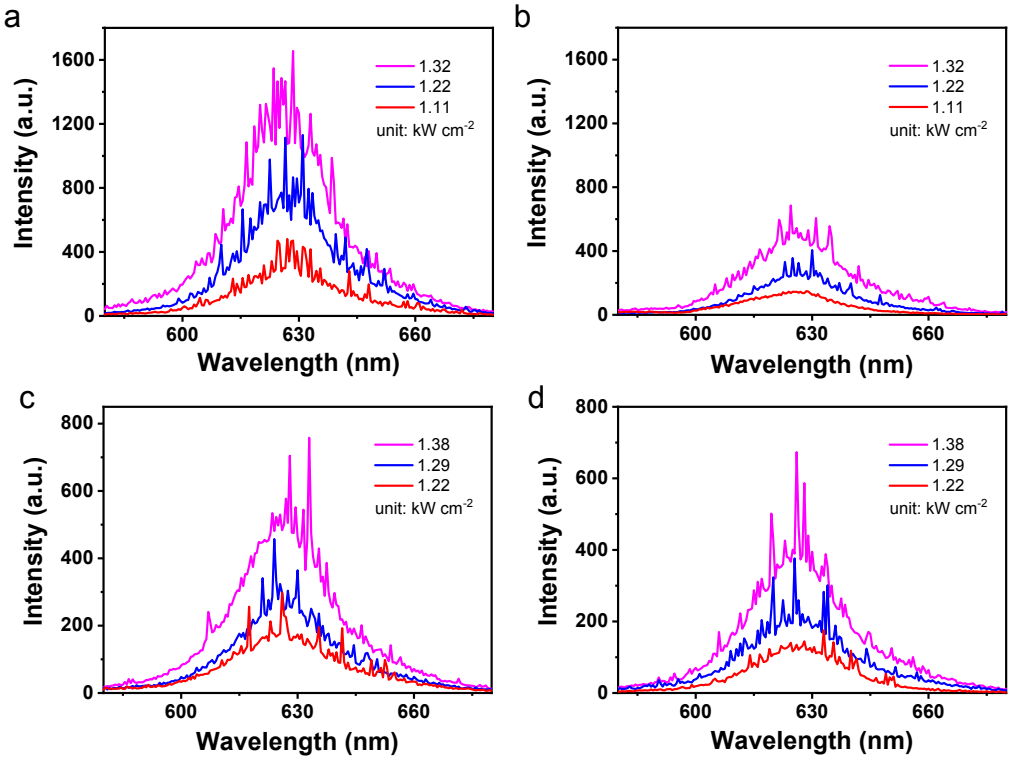

Figure S16 | The emission spectra of random lasing action for the GCHMM on (a) concave and (b) convex glass substrates under the curvature radius of 20 mm. (c) and (d) are corresponding under the curvature radius of 50 mm, respectively.

14. Emission performances after immersion in DI water.

Figures S17 shows the emission performances of GCHMM device after immersion in DI water up to 96 hours under the pumping energy intensity of 1.10 kW cm^{-2}.

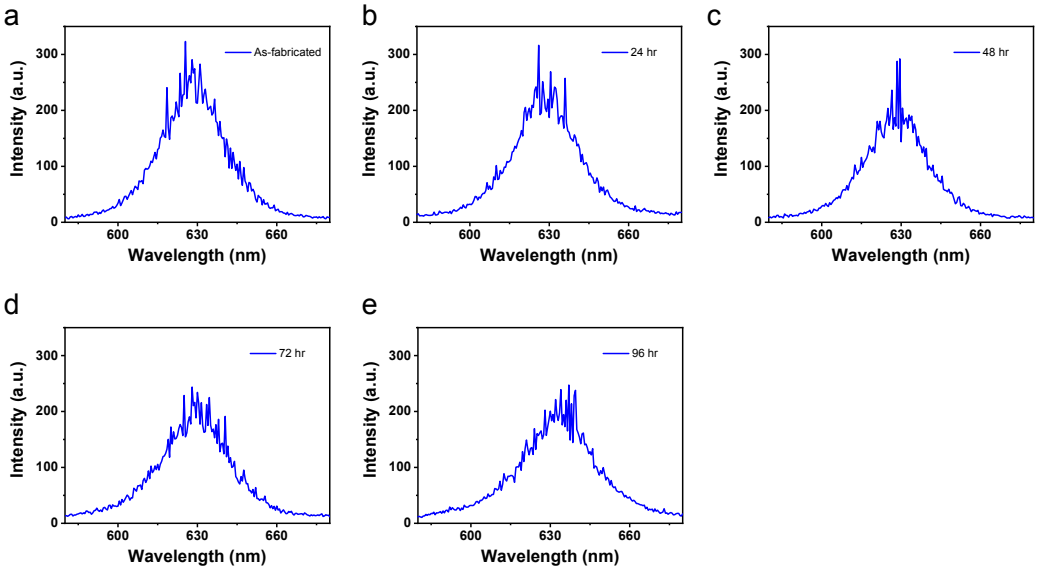

Figure S17 | The emission spectra of random lasing action for the GCHMM (a) as-fabricated, after immersion in DI water to (b) 24, (c) 48, (d) 72, and (e) 96 hours.

15. The simulation settings.

The simulation settings of scattering, PDOS, decay rates, and electric-field distribution are shown in Figs. S19–S22. The scattering efficiency (in Fig. 5a) is simulated as follows. We used grating or planar structures plane wave source, total-field scattered-field (TFSF), to simulate the scattering from a particle on different substrates (in Fig. S19). This TFSF, marked as a white box, which injects a plane from the top of the substrate with an electric-polarization (blue arrow) and a wave vector (pink arrow). The scattering monitor (yellow box) is placed at outside of the TFSF source to analysis the scattered net energy out from the grating or planar structures. Finally, this scattered net energy is divided by the geometrical area of grating or planar structures. From the XZ view, the green half-space area is anti-symmetric BC and from the YZ view, the blue half-space area is symmetric BC. The rest BCs are set as the PML, which are used to prevent the propagation back owing to the BCs to furtherly interact with the structure again. The mesh size in the whole simulations in this work is set as 1 nm, and the mesh accuracy is 7 (very high in FDTD).

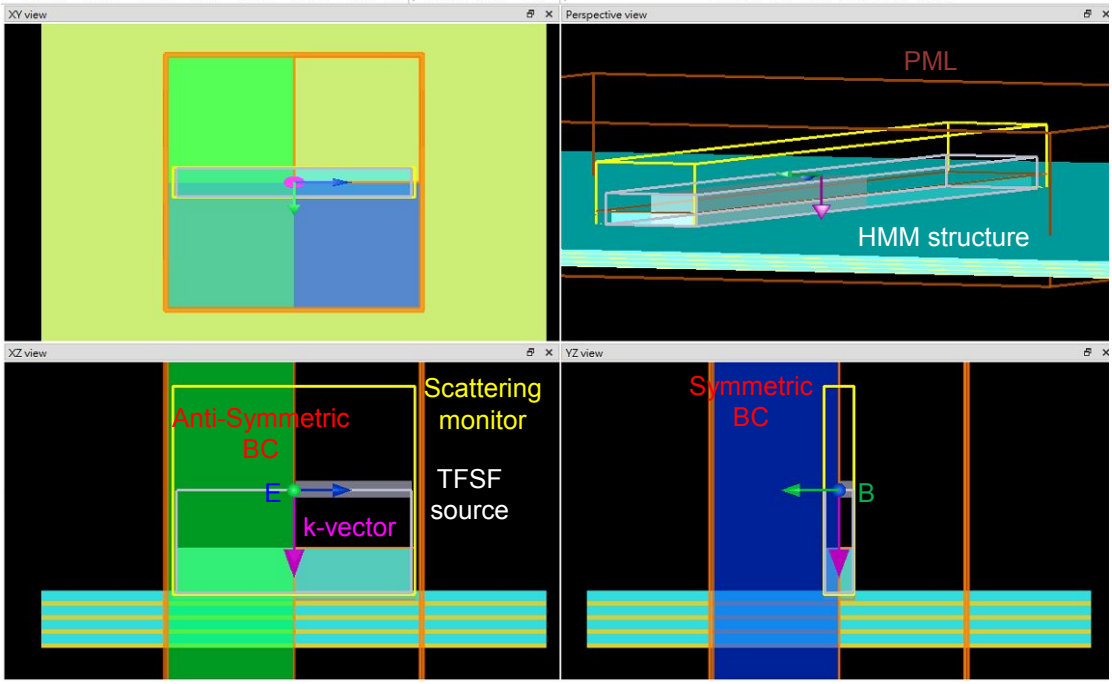

Figure S19 | 3D FDTD simulation for the scattering efficiency on GCHMM substrate. A particular plane wave source, TFSF is used to simulate the scattering from grating or planar structures on different substrates. This TFSF, marked as a white box, which injects a plane from the top of the substrate with an electric-polarization (blue arrow) and a wave vector (pink arrow). The scattering monitor (yellow box) is placed at outside of the TFSF source to analysis the scattered net energy out from the grating or planar structures. Finally, this scattered net energy is divided by the geometrical area of grating or planar structures. From the XZ view, the green half-space area is anti-symmetric BC and from the YZ view, the blue half-space area is symmetric BC. The rest BCs are set as the PML.

The photonic density of states (PDOS) and decay rates in Fig. 5a are simulated based on the isotropic dipole emitters on top of different substrates. The dipole emitters are composed of perpendicular (in Fig. S20) and parallel (in Fig. S21) dipole emitters to the substrates. The emission wavelength of the dipole emitters is set as 630 nm to

mimic the emission of QDs, and the distance is set at the central position of homogeneous QDs. Since the emission of QDs is isotropic, the PDOS and decay rates are determined from the perpendicular parallel dipole emitters to the substrates as:

$$isotropic = \frac{1}{3}\perp + \frac{2}{3}\parallel . \tag{S13}$$

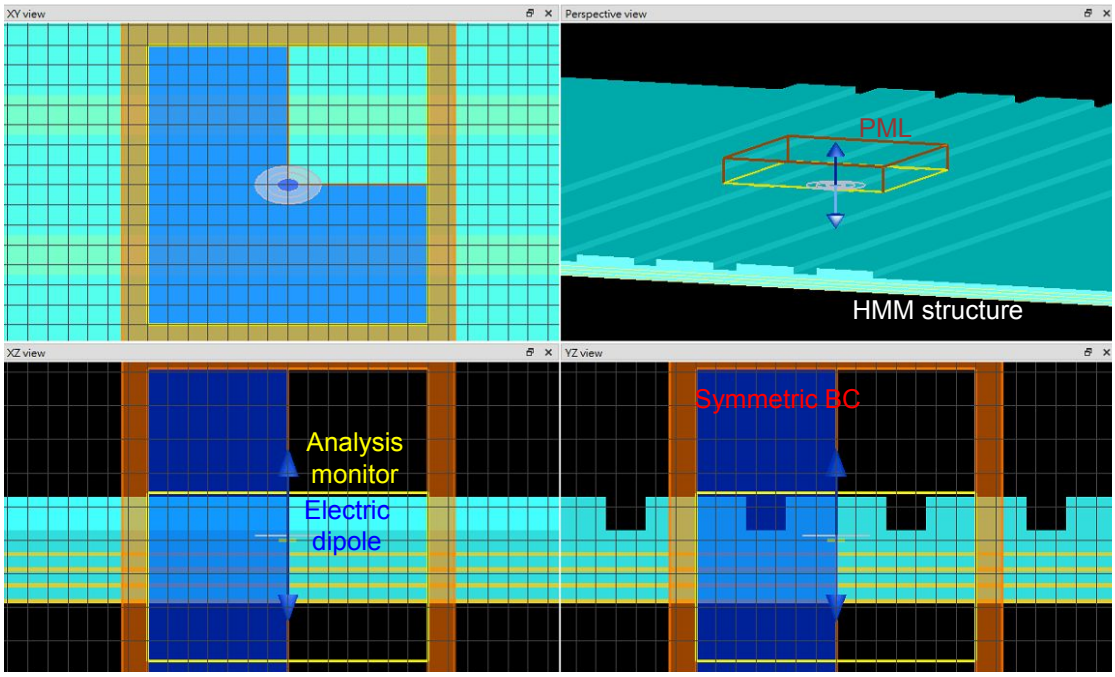

Figure S20 | 3D FDTD simulation for a perpendicular electric-dipole on GCHMM. The electric dipole perpendicular to the GCHMM is marked as a blue arrow. The blue half-space area is symmetric BC in the YZ view. The rest BCs are set as the PML.

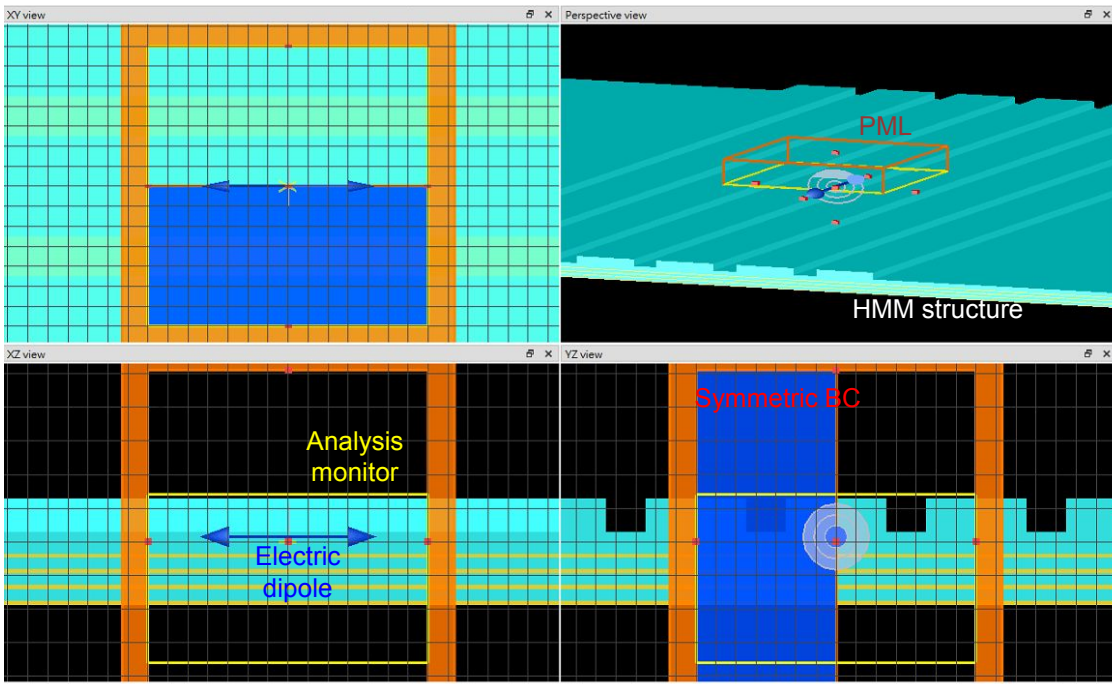

Figure S21 | 3D FDTD simulation for a parallel electric-dipole on GCHMM. The electric dipole parallel to the GCHMM is marked as a blue arrow. The blue half-space area is symmetric BC in the YZ view. The rest BCs are set as the PML.

The electric-field distribution for the GCHMM generated by the vertical dipole orientation is shown in Fig. S22.

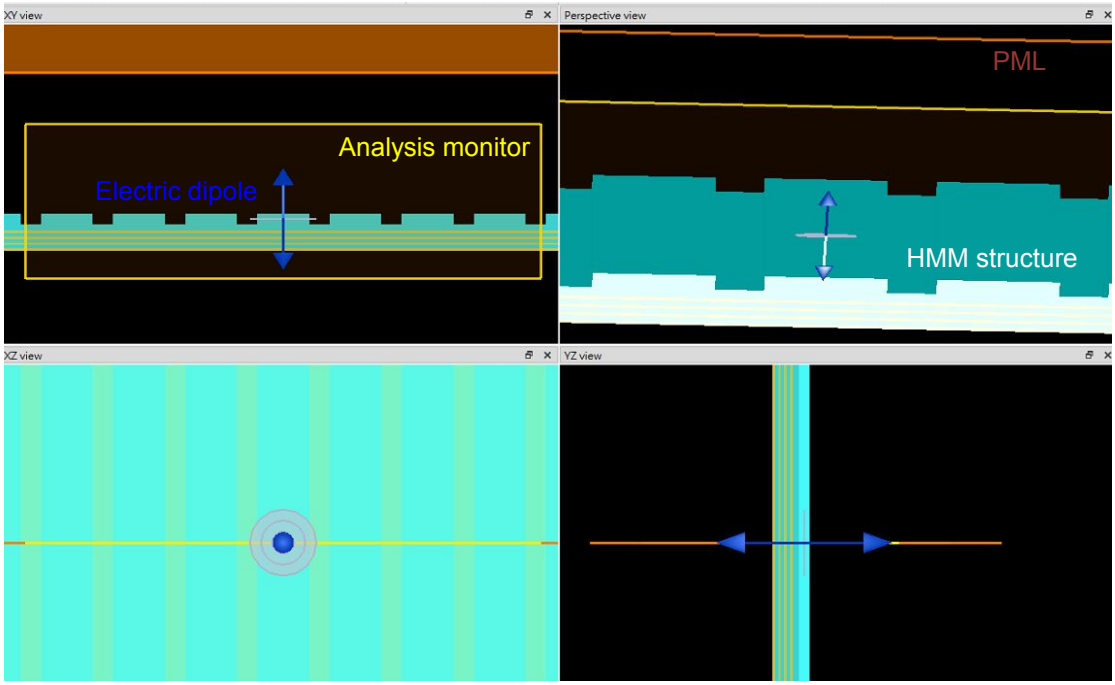

Figure S22 | 2D FDTD simulation to determine the electric-field distribution on GCHMM. The electric-field distribution for the GCHMM generated by the vertical dipole orientation

References

1. Cortes, C. L.; Newman, W.; Molesky, S.; Jacob, Z., Quantum nanophotonics using hyperbolic metamaterials. *J. Opt.* **2012,** *14* (6), 063001.

2. Poddubny, A.; Iorsh, I.; Belov, P.; Kivshar, Y., Hyperbolic metamaterials. *Nat. Photon.* **2013,** *7* (12), 948-957.

3. Ford, G. W.; Weber, W. H., Electromagnetic interactions of molecules with metal surfaces. *Phys. Rep.* **1984,** *113* (4), 195-287.

4. Barnes, W. L., Fluorescence near interfaces: The role of photonic mode density. *Journal of Modern Optics* **1998,** *45* (4), 661-699.

5. Walpole, J. N.; Kintzer, E. S.; Chinn, S. R.; Wang, C. A.; Missaggia, L. J., High-power strained-layer InGaAs/AlGaAs tapered traveling wave amplifier. *Appl. Phys. Lett.* **1992,** *61* (7), 740-742.